

The Elastic Effect of Evolving Precipitate Shapes on the Ripening Kinetics of Tetragonal Phases



FELIX SCHLEIFER, YUEH-YU LIN, UWE GLATZEL, and MICHAEL FLECK

Coherent tetragonal precipitates, such as the Ni_3Nb phase γ'' found in Ni-base superalloys, appear as plate-shaped particles. These shapes are the result of anisotropic elastic misfit strains. We present 3D sharp phase-field simulations that capture this circumstance well due to the inclusion of the elastic effects from the misfit. These simulations reveal that the ripening behavior of γ'' precipitates deviates significantly from the classical LSW theory of Ostwald ripening. A ripening exponent of 2 rather than 3 describes the simulated γ'' size evolution at temperatures between 700 °C and 760 °C best. Employing a quantitative distinction argument, we show that 60 pct of this deviation is attributed to the elastically induced size dependence of the precipitate shapes. With increasing precipitate size, the minimization of elastic energy leads to steadily increasing plate aspect ratios. The precipitate ripening kinetics accelerate with increasing aspect ratio. Fitting the newly received square root time dependence to experimental data yields a physically conclusive activation energy of ripening close to the activation energy of Nb diffusion in the alloy.

<https://doi.org/10.1007/s11661-022-06877-x>
© The Author(s) 2022

I. INTRODUCTION

NICKEL-BASE superalloys show extraordinary mechanical properties at temperatures above 600 °C mostly due to precipitation of intermetallic phases. Niobium-containing alloys, such as the widely used wrought alloy 718, are primarily strengthened by the metastable tetragonal γ'' phase with stoichiometry Ni_3Nb that is embedded in an fcc solid-solution matrix phase.^[1] The phase precipitates coherently or semi-coherently with a strongly anisotropic lattice misfit relative to the matrix phase. This anisotropy of the misfit causes the precipitates to form plate-shaped particles.^[2] The γ'' phase plays an important role in the development of novel wrought alloys for turbine applications as it can be used to deliberately inhibit coarsening of γ' precipitates.^[3–5] To study the formation of γ'' precipitates, a derivative of the commercial alloy 718 is used that is referred to as 718 M(odified).^[6] After heat treatment, the microstructure of alloy 718 M consists only of γ'' precipitates and the fcc matrix that have both compositions comparable to the phases found in alloy 718.^[7]

The compositions in wt pct of alloy 718 and its derivative 718 M are given in Table 1.

During long-term high-temperature exposure, the microstructure of Ni-base superalloys coarsens, meaning that the mean precipitate size increases. This effect plays an important role during the precipitation heat treatment as well as during service. The adjustment of heat treatment times provides an indirect design control on the precipitate size and during service as the increasing precipitate size ultimately leads to deterioration of the mechanical properties of the material. Understanding the mechanism of γ'' precipitate coarsening allows for the development of computational models that precisely describe the microstructure formation at elevated temperatures. In the context of integrated computational materials engineering such models are key to successful material development and process optimization.

The experimental temporal evolution of γ'' precipitate sizes during aging has been extensively studied under the assumption of classical ripening theory.^[8–14] The microstructural evolution of systems with tetragonal plate-shaped precipitates has been studied using a model for the nucleation, precipitation, and coarsening of γ'' precipitates in alloy 625 developed by Moore *et al.* The model reproduces experimental distributions of the precipitate size and aspect ratio.^[15] 2D Phase-field simulations revealed that aging under load leads to selective dissolution of γ'' precipitates depending on their orientation.^[16]

Fourth European Symposium on Superalloys and their Applications. FELIX SCHLEIFER, YUEH-YU LIN, UWE GLATZEL, and MICHAEL FLECK are with the Metals and Alloys, University of Bayreuth, Prof.-Rüdiger-Bormannstraße 1, 95447, Bayreuth, Germany. Contact e-mail: michael.fleck@uni-bayreuth.de
Manuscript submitted July 29, 2022; accepted October 21, 2022.
Article published online November 22, 2022

From a computational materials science perspective, the coarsening of microstructures is conveniently studied using the phase-field method. It provides a versatile framework to study phase transformations involving micro-mechanical effects as well as complex materials chemistry. Therefore, the phase-field method is a powerful tool for mesoscale simulation of microstructure evolution within the context of integrated computational materials engineering.^[17,18] Important examples for the application of the phase-field method to the field of precipitation microstructure evolution, are, for instance, the investigations of γ' rafting in nickel-based superalloys, as recently reviewed by Yu *et al.*^[19] A particular advantage of the phase-field method in this respect is its ability to predict the complex shaping of mechanically interacting particles.^[20–22] However, here, we consider the application of the phase-field method to the ripening behavior of precipitates involving cubic to tetragonal transformations.^[23,24] In this case, we benefit from the ability of the method to predict meaningful particles shapes under the quasi-equilibrium conditions at realistic precipitate phase fractions.^[25,26]

In this work, we investigate the deviation of γ'' precipitate ripening behavior in the alloy 718 M from classical ripening laws. We measure the ripening exponent from conclusive 3D phase-field simulation data. The observed ripening behavior is validated by comparison of activation energies of ripening from experimental aging data to the activation energy of Nb diffusion. By extending classical ripening laws to include size-dependent ripening kinetics, we derive an argumentation that allows to quantitatively separate the elastic effects that influence the ripening exponent.

Table I. Composition of Alloys 718 and 718 M in Wt Pct

Alloy	Al	Ti	Cr	Fe	Co	Ni	Nb	Mo
718	0.5	0.9	18	18 (bal.)	0.3	54.8	5.0	3.0
718 M	—	—	18	16 (bal.)	—	58.0	5.0	3.0

II. THE γ'' PRECIPITATE MICROSTRUCTURE

A. The Size-Dependent γ'' Precipitate Shape

Figure 1(a) shows a schematic drawing of the elastic lattice distortion around a plate-shaped γ'' precipitate caused by the lattice misfit between precipitate phase and matrix. The misfit is exaggerated by a factor of 20. The grid is used to visualize misfit strains and does not necessarily reflect unit cells of the crystal. The anisotropy of the lattice misfit becomes evident when the top surface of the plate-shaped precipitate with an interface normal parallel to the crystallographic \bar{c} direction of the precipitate phase (Figure 1(b)) is compared to the circumferential interface of the plate normal to \bar{a} (Figure 1(c)). The dashed lines indicate the position of an ideal interface and the dots correspond to lattice sites that are in the view plane (large dots) or half a lattice plate behind (small dots). Black dots indicate Ni sites and white dots indicate Nb sites in the ordered γ'' phase. The gray dots indicate sites that are statistically occupied by the elements that form the unordered fcc matrix. The structure of the two given interfaces is clearly distinguishable and is found to show a strongly anisotropic misfit $\varepsilon_c \gg \varepsilon_a > 0$ with $\varepsilon_c/\varepsilon_a$ up to a factor of 60.^[27,28] Due to tetragonal symmetry, the lattice misfit in out-of-plane direction ε_b is equal to ε_a .

The morphology of the γ'' microstructure is strongly influenced by the interplay between the elastic lattice strain due to the misfit and the energy density of the matrix/ γ'' interface σ . The shape of these precipitates minimizes the sum of interfacial and elastic energy.^[29] The elastic bulk driving force of the precipitate shape formation leads to the plate shape as it favors interface formation normal to the crystallographic direction of the largest misfit, the \bar{c} -direction. The equilibrium precipitate shape is an oblate spheroid.^[2] This is a sphere that is compressed along the \bar{c} -direction by a factor of A , the aspect ratio. At high precipitate volume fractions elastic interaction between precipitates leads to deviation from the spheroidal shape.^[25,30] The

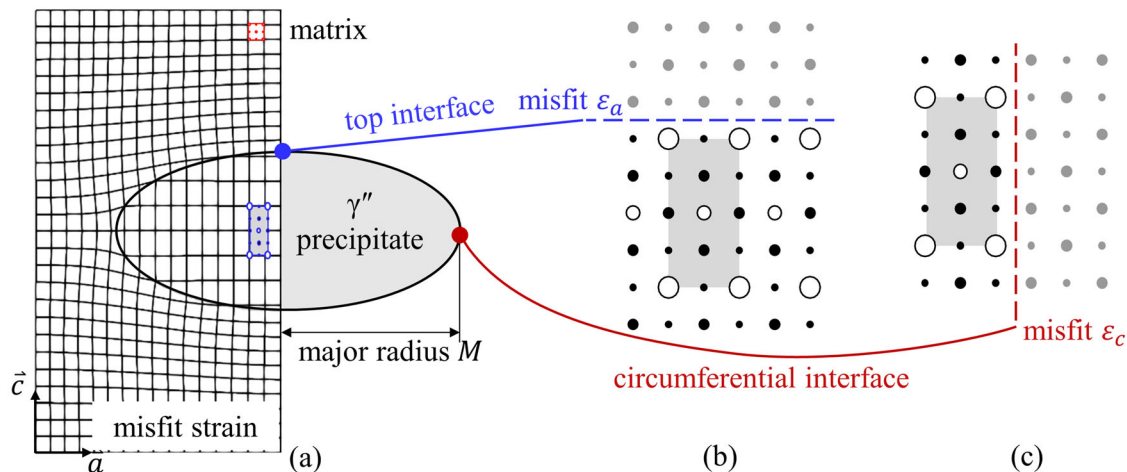


Fig. 1—The anisotropic matrix/ γ'' interface. (a) lattice misfit strains around a γ'' precipitate exaggerated by a factor of 20. (b) Crystallographic structure of the top interface normal to \bar{c} and (c) of the circumferential interface normal to \bar{a} .

precipitate size is usually described by the plate diameter that is twice the major radius M of the precipitate as shown in Figure 1(a). To describe the precipitate size independently of the precipitate shape, the equivalent radius R is used. It is defined as the radius of a sphere with the same precipitate volume. Major radius and equivalent radius are related via $M^3 = R^3 A$.^[31]

Reduction of interfacial energy causes the precipitates to be compact while reduction of elastic energy leads to the formation of the plate shape. The ratio between the bulk elastic driving force and the interfacial energy is size dependent and thus the tendency towards plate formation depends on the precipitate size. The shape formation of smaller precipitates is mostly driven by interface reduction and therefore the precipitates tend to be more spherical when the interfacial energy is assumed to be isotropic. When γ'' precipitates grow, the volume increases faster than the interfacial area and thus interfaces normal to \bar{c} become more favorable. This leads to an increasingly pronounced plate shape with increasing precipitate size. The aspect ratio A of the plate-shaped particles is a function of the dimensionless ratio Q between the elastic energy scale of the system and the interfacial energy scale.^[28] In the special case of γ'' precipitates in the alloy 718, this ratio can be sufficiently approximated by

$$Q = \frac{C_{44}^p \cdot \varepsilon_c^2}{\sigma} R, \quad [1]$$

where R is the equivalent radius of the precipitate, C_{44}^p is the shear modulus of the precipitate phase, σ is the isotropic interfacial energy density, and ε_c is the largest entry of the anisotropic eigenstrain tensor that represents the lattice misfit.^[30] This is because the anisotropy in the elastic energy imposed by an γ/γ'' interface is proportional to the squared ratio between the large and the small misfit. As such it dominates the other anisotropic driving forces for shape formation that are the anisotropy of the interfacial energy, anisotropy of interface mobility, and inhomogeneity of the elastic constants by orders of magnitude.^[30] The ratio Q can also be understood as a dimensionless precipitate size, normalized by a characteristic length scale $L = \sigma / (C_{44}^p \varepsilon_c^2)$.^[32] Between 700 °C and 760 °C, we find the following values, $\varepsilon_c = 30 \times 10^{-3}$,^[28] $C_{44}^p = 100$ GPa,^[33] and $\sigma = 0.18$ J m⁻².^[31] This leads to $L = 2$ nm. The size-dependent precipitate shape is now defined by the aspect ratio $A(Q)$.

B. Ostwald Ripening of γ'' Precipitates

Figure 2 shows scanning electron microscopy images of the matrix/ γ'' microstructure in a single crystal of alloy 718 M.^[25] The samples are etched to reveal the full precipitates. The increase of precipitate size and aspect ratios is distinctively visible. The determined mean plate diameters after 2, 6, and 10 hours of aging are 40, 80, and 100 nm, respectively.

Over long durations of increased temperature, Ostwald ripening is the dominating cause of microstructure coarsening. When the precipitate phase is close to the equilibrium phase fraction, the growth of precipitates is driven by the reduction of the total interface area. Assuming isotropic interfacial energy density σ and no lattice misfit, the Gibbs–Thomson effect leads to an increase of the Nb diffusion potential μ_{Nb} in the matrix around the phase boundary via

$$\Delta\mu_{Nb} \propto \sigma\kappa, \quad [2]$$

where κ is the local curvature of the interface.^[34] In the case of spherical precipitates, κ is the inverse radius of the precipitate. This increase of the diffusion potential leads to a mass flow of Nb from small precipitates with large κ to larger ones. Small precipitates dissolve and larger ones grow on their behalf. The classical description of Ostwald ripening is the LSW theory in the form of

$$\bar{R}(t)^3 - \bar{R}(t_0)^3 \propto t - t_0, \quad [3]$$

where \bar{R} is the arithmetic mean of the radius R of all precipitates in the system at the time t .^[35,36] $\bar{R}(t_0)$ is the mean radius at the reference time t_0 . The original solution to Ostwald ripening considers spherical particles and thus the radius (or diameter) of the particles is the appropriate choice to measure the particle size. Particle sizes of strongly anisotropic shapes, such as γ'' precipitates, can be defined differently. Equation [3] or related descriptions for microstructural evolution of γ'' are often applied to either the plate diameter^[8] or to an equivalent radius of a sphere with the same volume as the precipitate.^[15,37,38]

The temporal evolution of \bar{R} is governed by a cube root function

$$\bar{R}(t) = \sqrt[3]{K(t - t_0) + \bar{R}(t_0)^3}, \quad [4]$$

where K is the ripening coefficient. K is a function of the diffusivity and solubility of the precipitate forming elements in the matrix phase, the interfacial energy density, and temperature.^[35,36] It is determined as the slope of a plot of \bar{R}^3 over t . The root like time dependence of the precipitate size is visible in Figure 2 as the increase in precipitate size is much more pronounced between Figures 2(a) and (b) (after 2 and 6 hours) than between (b) and (c) (6 and 10 hours).

The ripening kinetics are strongly temperature dependent due to their diffusional nature. The temperature dependence of the ripening kinetics is dominated by the temperature dependence of the diffusivities of the alloying elements. The temperature dependence of the solubility of the elements in the matrix phase and the interfacial energy density are non-zero but are less pronounced than the temperature dependence of the diffusivities. The temperature dependence of the ripening coefficient K can be expressed as

$$KT \propto \exp\left(-\frac{E_R}{RT}\right), \quad [5]$$

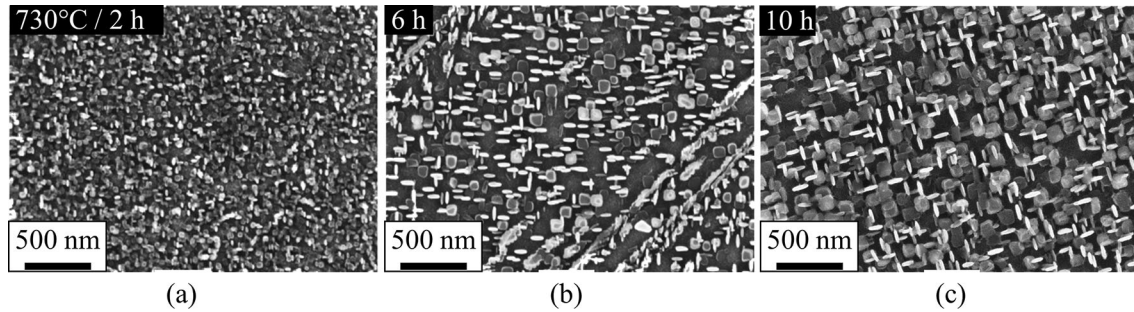


Fig. 2—Ripening of γ'' precipitates in alloy 718 M. SEM images after (a) 2, (b) 6, and (c) 10 hours of aging at 730 °C. Adapted from reference,^[25] under the terms of the Creative Commons CC BY license.

Table II. Activation Energies of Diffusion for the Alloying Elements in Alloy IN718M

Element	Alloy	E_D in kJ mol^{-1}	References
Nb	718	237	40
Nb	718	257	41
Nb	718 M	258	39
Cr	718 M	278	39
Fe	718 M	286	39
Mo	718 M	281	39

with E_R being the activation energy of ripening and R_G being the universal gas constant. The activation energy of ripening E_R is measured from the slope of a plot of $\ln(KT)$ over the inverse temperature T^{-1} .^[8] The observed activation energy of ripening is a direct consequence of the activation energy of diffusion that describes the mobility of the alloying elements. A physically meaningful activation energy of ripening is therefore identical to the activation energy of diffusion of the elements that form the precipitates. Activation energies of diffusion of the alloying elements in alloy 718 M from the mobility database MobNi4^[39] are given in Table II together with experimental activation energies of Nb diffusion in alloy 718.

The LSW theory of Ostwald ripening is valid only under certain conditions. The LSW theory assumes negligible precipitate volume fraction and thus no interaction between precipitates via the depletion fields around them. Also, no coalescence of precipitates is considered. The precipitates are assumed to be spherical. Deviation from these assumptions do not change the qualitative time dependence of the precipitate size evolution but rather increases the ripening coefficient and changes the shape of the precipitate size distribution.^[42] Under the assumption of the classical LSW cube root time dependence, extraordinarily high activation energies can be observed^[43,44] as well as a strong scatter of the determined ripening coefficients.^[8] These inconsistencies indicate short comings of the LSW theory for γ'' size development. Abnormally high activation energies can be explained by delayed homogenous nucleation of γ'' .^[43]

The LSW theory is also only valid for stress-free systems. Elastic misfit strains caused by coherent precipitation of ordered phases can significantly change the ripening behavior of intermetallic phases in alloys such that the cube root time dependence of the LSW theory does not hold.^[45] A generalized approach to describe the time evolution of arbitrarily defined precipitate sizes $S \in [M, R]$ is to assume an apparent ripening exponent $n \leq 3$ such that

$$\overline{S}(t)^n - \overline{S}(t_0)^n = K(t - t_0) \quad [6]$$

with the ripening coefficient K that has the dimension of a length to the n -th power over time. The ripening exponent n distinguishes between ripening behaviors of systems, while the coefficient K is a measure for the kinetics of systems that behave equally. A ripening exponent of 2.3 was found to describe the ripening behavior of cuboidal γ' precipitates in 2D simulations of a Ni-base superalloy with high precipitate volume fraction.^[45] A reduction of the ripening exponent due to misfit stresses is reported.^[46] When trans-interface diffusion, and not bulk diffusion, is ripening rate controlling, the ripening exponent is found to be $n = 2$.^[47] The deviation from $n = 3$ becomes increasingly pronounced when elastic effects become increasingly dominant.^[32] The observation that lattice misfit stresses reduce the ripening exponent is independent of the precipitate shapes.

Kim & Voorhees modeled the ripening behavior of spheroidal precipitates in a stress-free system and found that, assuming constant aspect ratios, the ripening exponent of 3 is conserved. This is in good agreement with the finding that the ripening exponent of 3 is also conserved for cuboidal precipitates.^[48] Non-spherical precipitate shapes alone do not lead to a deviation of the ripening exponent. However, an increase of the ripening coefficient K with increasing aspect ratio A was observed for cylindrical precipitate shapes^[49,50] and for spheroidal precipitates^[38] relative to spherical precipitates of the same volume. Cubic precipitates with isotropic misfit exhibit a shape transition from cubes to cuboidal plates at low volume contents.^[51] Coarsening of systems of cuboidal plates with phase-field models revealed deviations from classical ripening behavior. Especially the

time evolution of plate radius and thickness differs significantly.^[52,53] The mean equivalent radius of the precipitates increases with an exponent of 2.4.^[53] Analytically it can be shown that the mean plate radius of plate-shaped melt inclusions also increases with a reduced exponent of 2.4 due to local stresses.^[54]

With an increasing precipitate aspect ratio, the total mean curvature of the interface increases compared to the curvature of a spherical particle with equal volume. This is a purely geometrical effect. When the precipitate shape is caused solely by an anisotropy of the interfacial energy, rather than anisotropic misfit strains, the inverse effect can be observed.^[38] Needle-shaped precipitates also show the inverse effect of inhibited growth kinetics compared to spherical precipitates.^[50]

Considering the size dependence of the precipitate shape, namely of the aspect ratio of plate-shaped precipitates, together with the shape dependence of the ripening coefficient, significant deviation from the classical ripening behavior is observed.^[31] When the aspect ratio increases during ripening, the ripening kinetics are accelerated. This causes an ever-increasing ripening coefficient.^[26] This effect was observed in 3D phase-field simulations of γ'' ripening. The mean precipitate size does not increase with an exponent of 3 but rather with a decreased exponent.^[31] This effect is induced by the elastically induced shape formation of the precipitates and is clearly separable from the effect that elastic stresses have on the ripening behavior independently of the precipitate shape.

III. METHODOLOGY

The ripening behavior of the γ'' phase in Ni-base superalloys is studied using sharp phase-field simulations together with controlled, ex-situ aging experiments. An experiment has the advantage, that it naturally provides fully realistic precipitate microstructure evolution. However, in the ex-situ experiment it is not possible to get continuous information on the evolutionary state of the same particular area of the material microstructure. Every data point corresponds to a distinct aging experiment with a distinct sample. The aging has to be interrupted and each sample has to be prepared for subsequent scanning electron microscopy (SEM) analysis. In contrast to this, the 3D sharp phase-field simulations do allow the time-continuous, in-situ access to the evolution of a particular microstructural state.

A. Sharp Phase-Field Modeling of Microstructure Evolution

Just as usual phase-field models, the sharp phase-field model is based on the definition of the phase-field parameter φ , to locally discriminate the phase state of the material. A numerical value of $\varphi = 0$ corresponds to the matrix phase, $\varphi = 1$ corresponds to the precipitate phase and all values in between are possible within the diffuse interface regions, located in between the two phases. The sharp phase-field model overcomes spurious

grid friction, grid pinning as well as substantial amounts of grid anisotropy, which all together seriously limit the resolution efficiency of the conventional phase-field models.^[55] The important novelty of the sharp phase-field model is that it is formulated in terms of an entirely discrete theory, taking into account the discrete nature of the numerical solution.^[56] We start from the ideal interface profile with phase-field values φ_i at discrete sites in the computational grid i

$$\varphi_i = \frac{1}{2}(\tanh(i\Delta x + x_0) + 1). \quad [7]$$

Here, Δx is the physical grid spacing of the discretization, x_0 is the position of the interface between two numerical grid points. The interface is defined as the point (in higher dimensions the iso-surface) where $\varphi = 1/2$.

Let the discrete grand potential be defined as the sum over all numerical grid points with their respective Cartesian coordinates \vec{x}_i

$$\Omega = \Delta x^3 \sum_i \omega_{int}(\vec{x}_i) + \omega_{bulk}(\vec{x}_i). \quad [8]$$

The isotropic interfacial contribution ω_{int} consists of two terms. The first assigns an energy amount to the squared magnitude of the gradient of the phase field and thus causes a widening of the phase boundary. The second term is a double-well potential p with minima at 0 and 1. Thus, wide interfaces are energetically penalized, and the interface width approaches 0. To obtain a constant, defined interface, both terms are suitably weighted. The result for the interface contribution is

$$\omega_{int} = \frac{\sigma}{\sigma_0} \left(\frac{1}{2} |\tilde{\nabla} \varphi_i|^2 + p(\varphi_i) \right), \quad [9]$$

where σ is the physical isotropic interfacial energy density and σ_0 is a reference interfacial energy density, which results from the definition of the potential p and the gradient term. The essence of the sharp phase-field model is a specifically modified potential landscape, which is easily integrated into our previous finite difference phase-field implementations.^[26,30] The following potential is obtained:

$$\frac{p(\varphi_i)}{p_0} = \frac{4\varphi_i(1-\varphi_i)}{(\Delta x)^2} + \frac{1 - \tanh^2(\Delta x)}{(\Delta x)^2 \cdot \tanh^2(\Delta x)} \cdot \ln \left(\frac{1 - \tanh^2(\Delta x)}{1 - \tanh^2(\Delta x)(1 - 2\varphi_i)^2} \right). \quad [10]$$

The discrete gradient operator is defined as

$$|\tilde{\nabla} \varphi_i|^2 = \sum_{j=1}^3 \frac{3\rho_j}{\psi_j j(\Delta x)^2} \sum_{k=1}^{\psi_j} \left(\varphi(\vec{x}_i + \vec{x}_{jk}) - \varphi_i \right)^2, \quad [11]$$

where the index j indicates the neighborhood shell (1st, 2nd, and 3rd neighbors), ρ_j is the weighting factor of

shell j , and ψ_j is the coordination number of this shell, *i.e.*, $\psi_1 = 3$, $\psi_2 = 6$, and $\psi_3 = 4$.^[55,56] For the weighting factors $\sum \rho_j = 1$ holds. The index k is a numerator over the ψ_j neighbors within a shell and \vec{x}_{jk} is the direction vector to the k -th neighbor in the j -th shell. The following parameters were found to provide minimized spurious anisotropy: $\rho_1 = 0.4130$, $\rho_2 = 0.1539$ and $\sigma_0 = 0.2945$.^[55] This sharp phase-field formulation on a simple cubic computational grid provides a dimensionless interface profile width of 2 and globally restores translational invariance in 100 directions of the computational grid.^[55]

The bulk energetic contributions to the grand potential density of Eq. [8] are the local elastic strain energy $\omega_{el}(\varphi, \vec{u})$ and the chemical energy $\omega_{ch}(\varphi, \mu)$. The corresponding state variables are the displacement field \vec{u} and the Nb diffusion potential field μ . The latter works well with the sharp phase-field formulation as it is continuous across the interface. To consider phase-dependent volume contributions to the local energy density, the interpolation function $h(\varphi) = 3\varphi^2 - 2\varphi^3$ is used. The anisotropic misfit is modeled as an eigenstrain $\vec{\varepsilon}_0 = (\varepsilon_a, \varepsilon_a, \varepsilon_c)$ of the precipitate phase. The tensors of elasticity C of both phases are anisotropic. The local strain state ε is derived from the displacement field that is solved in every time step of the simulation.^[57] The elastic contribution to the phase-field energetics is then

$$\omega_{el} = \frac{1}{2}(\varepsilon - \vec{\varepsilon}_0)\overline{C}(\varepsilon - \vec{\varepsilon}_0), \quad [12]$$

where $\vec{\varepsilon}_0$ and \overline{C} are the phase-dependent elastic parameters interpolated with $h(\varphi)$.

The diffusional nature of the microstructure development is reflected in the chemical bulk energy contribution $\omega_{ch}(\varphi, \mu) = h(\varphi)\omega_{ch}^{\gamma''} + h(1 - \varphi)\omega_{ch}^{\gamma}$. The grand potential landscape of the considered phases $\alpha \in (\gamma, \gamma'')$ as a function of the local concentration of Nb $c(\vec{x}_i)$ is approximated parabolically as follows:

$$\omega_{ch}^{\alpha} = \frac{1}{2}(c - X_{\alpha})^2\chi_{\alpha} + Y_{\alpha} - \mu c. \quad [13]$$

The coordinates of the vertex of the parabola are X_{α} and Y_{α} . The thermodynamic factor χ_{α} can be understood as the inverse solubility of Nb in the phases.^[45] These phase-dependent parameters couple directly to CALPHAD thermodynamics.^[57] The last term in Eq. [13] comes from the Legendre transformation from Gibbs energy to grand potential energy.^[57] The local concentrations can be calculated from the diffusion potential field via

$$c(\vec{x}_i) = (\chi_{\alpha})^{-1}\mu(\vec{x}_i) + X_{\alpha}. \quad [14]$$

The temporal evolution equations of the phase field, the diffusion potential field, and the displacement field are derived directly from the discrete grand canonic potential functional by means of variational principles as

$$\frac{\partial \varphi}{\partial t} = -\frac{2M_{IF}}{3\Gamma\xi} \frac{\delta\Omega}{\delta\varphi}, \quad [15]$$

$$\frac{\partial}{\partial t} \left(\frac{\delta\Omega}{\delta\mu} \right) = M_{Nb} \nabla(\nabla\mu), \quad [16]$$

$$\frac{\delta\Omega}{\delta u_i} = \frac{\partial}{\partial x_i} \frac{\partial \omega_{el}}{\partial \varepsilon_{ij}} = 0, \quad [17]$$

where M_{Nb} is the mobility of Nb and a function of the diffusivity D_{Nb} and of the thermodynamic factor χ_{α} . M_{IF} is the mobility of the interface that is chosen to be $3D_{Nb}$ to ensure diffusion-limited phase-field kinetics. The evolution equations are given explicitly in the work of Mushongera *et al.*^[45] and Fleck *et al.*^[57]

3D simulations are used to investigate the ripening behavior of the γ'' phase at 730 °C. The simulation setup is chosen to reflect the aging experiments of Figure 2. Simulations were conducted on a numerical grid of 160^3 grid points which corresponds to a physical length of the simulation domain of 640 nm ($\Delta x = 4$ nm). The numerical time step is 0.01 s. The simulations are initialized with 300 precipitates randomly distributed in space at an equilibrium volume content of 10 pct.^[58] Periodic boundary conditions are applied to the phase field and the diffusion potential field. The elastic displacement field is subjected to plane-deformation boundary conditions that do not impose spurious external strain.^[30,31] The necessary material data are given in Table III. The interfacial energy density was calibrated to reproduce experimental precipitate shapes and the diffusivity was calibrated to reproduce experimental ripening kinetics at 730 °C.^[31] The tensor of elasticity of the two considered phases has 3 and 6 independent entries which reflects the cubic symmetry of the matrix and the tetragonal symmetry of the precipitate phase, respectively. Thermodynamic input data are taken from the databases TCNi8 and MobNi4.^[39]

To evaluate elastic effects on the ripening behavior, we conduct two comparable simulations: One that accounts for the elastic misfit strains and the other with vanishing eigenstrains in all directions. In the latter case, the precipitates are almost perfectly spherical. Only in the very rare case of particle coalescence or near particle coalescence with a strong depletion of Nb in the surrounding matrix around, we observe for a short period of time transient non-spherical shapes.^[31] When the anisotropic misfit is considered, the precipitates exhibit the expected plate shape. Precipitate size and aspect ratio are measured from the phase field with high precision by the method of second-order moments.^[31]

Table III. Phase-dependent Material Data for Phase-Field Simulation of γ'' Ripening at 730 °C

Material Parameter	Value	References
Lattice Misfit		
ε_a	1.2×10^{-3}	28
ε_c	30×10^{-3}	
Elastic Constants of the Matrix Phase		
C_{11}	200 GPa	30
C_{12}	150 GPa	
C_{44}	90 GPa	
Elastic Constants of the Precipitate Phase		
C_{11}	245 GPa	33
C_{33}	265 GPa	
C_{12}	150 GPa	
C_{13}	130 GPa	
C_{44}	100 GPa	
C_{66}	90 GPa	
Interfacial Energy Density		
σ	0.18 J m^{-2}	31
Nb Diffusivity		
D_{Nb}	$2.5 \times 10^{-17} \text{ m}^2 \text{ s}^{-1}$	31

B. Ex-Situ Aging Experiments

Aging experiments were carried out with alloy 718 M, which only includes the cubic matrix phase and the tetragonal γ'' precipitate phase.^[6,7] The carefully produced samples allow for direct comparison to the phase-field model as no additional phases are present that might interact with the γ'' phase or that might work as Nb sink. Pre-alloyed ingots were produced in an arc melting furnace under 500 mbar argon atmosphere, using pellets of the pure elements with > 99.99 pct purity. The material was cast as a single crystal in a proprietary Bridgman investment casting furnace (built by chair of Metals and Alloys, University of Bayreuth, Germany) with a spiral grain selector^[25] and was subsequently homogenized for 24 hours at 1150 °C followed by water quenching. This treatment effectively dissolves Nb segregations and avoids precipitation of other phases.^[7] After the solution heat treatment, the samples were aged for 2, 6, and 10 hours at 700 °C, 730 °C, and 760 °C to study the time and temperature dependence of γ'' size evolution.

Samples for scanning electron microscopy (SEM) were mechanically ground, polished with silica suspension, and the matrix phase was electrolytically etched with phosphoric acid solution (3 pct H_3PO_4) at 5 V. Microstructure images were taken with a SEM 1540EsB (Zeiss, Germany) with a column-near secondary electron detector (Z-contrast). By means of image segmentation and analysis of the second-order moments of the precipitates γ'' precipitate shapes and sizes are precisely measured in a way that allows consistent comparison to 3D simulation data.^[31] To ensure applicability of this method the samples are oriented with one crystallographic 001-direction of the single crystal parallel to the electron beam. To measure precipitate sizes and aspect ratios, the images were binarized with a neural network trained on images of γ'' precipitates. The binary images were then analyzed using the method of second-order moments.^[31] Precipitates that touch the boundary of the image are not fully visible, and are excluded from the

analysis. For every aging time and temperature, the arithmetic means over the precipitate size measures R and M were calculated.

IV. RESULTS AND DISCUSSION

A. Simulation Results

Figure 3 shows the simulated matrix/ γ'' microstructure at four time steps. Figure 3(a) and (e) shows the randomly generated initial microstructure consisting of spheres and ellipsoids with an aspect ratio of 3, respectively. In both cases, the mean volume of the precipitates is equal. In Figures 3(a) through (d), the spherical shape of the simulation without elastic driving forces is clearly visible. Figure 3 (e) through (h) shows the microstructure with plate-shaped morphology during the same simulated aging time. The initial condition reflects the artificially generated microstructure that is lost quickly due to a strong energetic preference in particle arrangement^[30] and due to the formation of a size distribution that is typical for precipitate ripening. The simulations of aging are limited to a time interval, where in both simulations the existence of over 90 precipitates is guaranteed. This yields 4.5 hours of simulated of 3D ripening data. Simulation of longer times is possible but more costly as they require larger simulation domains.

Figure 4(a) shows the mean precipitate size from the two simulations of γ'' ripening at 730 °C as a function of the simulated aging time t . For the plate-shaped precipitates, we compare two common measures of the precipitate size. In blue, we show the mean major radius \bar{M} that is half the plate diameter. In red, we show the mean equivalent radius \bar{R} of a sphere with the same volume as the precipitate. This latter measure is independent of the precipitate shape and represents the mass of a precipitate more precisely than \bar{M} . Both size measures are graphically explained in the inset to

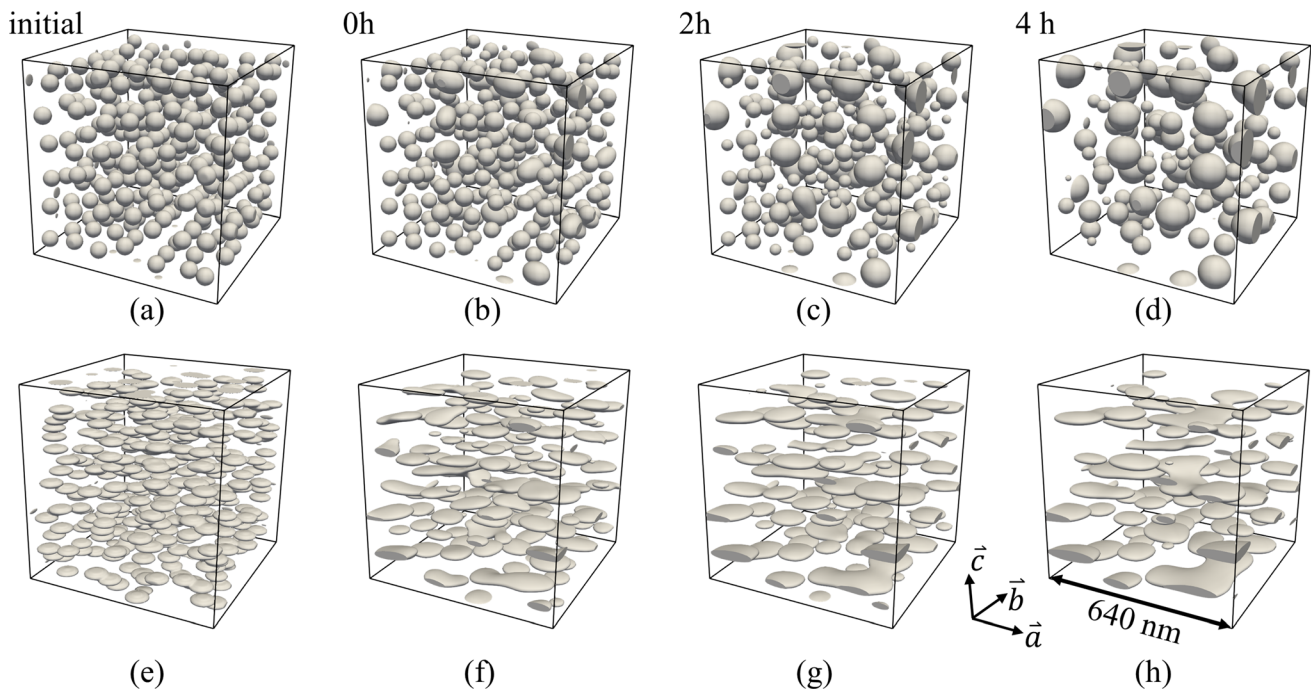


Fig. 3—Simulated 3D microstructure at different aging times. (a) to (d) without and (e) to (h) with consideration of elastic misfit strains.

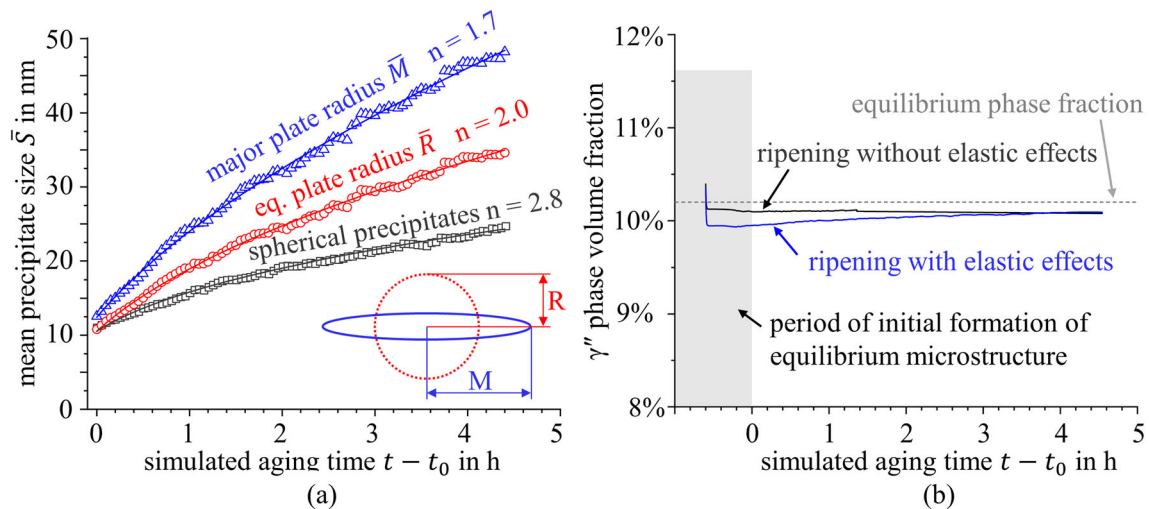


Fig. 4—(a) Mean precipitate size of plate-shaped and spherical γ'' precipitates with apparent ripening exponents n . (b) Evolution of the γ'' phase fraction during the simulation.

Figure 4(a). The equivalent radius \bar{R} of a precipitate is calculated directly from the precipitate volume. The major plate radius M and the aspect ratio A are calculated from best-fit ellipsoids.^[31]

Figure 4(b) shows the γ'' phase fraction over the simulated aging time. After initialization, the phase fraction drops due to the Gibbs–Thomson effect because the diffusion potential field is initialized homogeneously.^[45] The starting time t_0 is chosen such that the initial period of equilibrium microstructure formation is not included in the simulated aging to avoid bias from the initial conditions. The equilibrium phase fraction of

10.2 pct taken from the Calphad input data is shown as a dashed gray line. For both simulations, we find a relatively constant phase fraction. This is an important measure to show that in this simulation only the long-term coarsening by Ostwald ripening is observed.^[26] Both simulations show fractions that are slightly lower than the equilibrium phase fraction due to the surface pressure of the precipitates. With decreasing interfacial area this deviation vanishes. The simulation with plate-shaped precipitates due to elastic misfit strains shows stronger deviation from the equilibrium phase content due to increased interfacial area and due

to the elastic driving force that additionally acts on the interface.

From Figure 4(a) it becomes evident that the lattice misfit has a significant influence on the ripening behavior. The increase in precipitate size after 4 hours of aging is considerably larger when the elastic effects are considered. When the major radius M of the plates, rather than an equivalent radius R , is measured, we again observe increased precipitate growth. The size dependence of the precipitate shapes is implicitly visible as $\bar{R}(t)$ and $\bar{M}(t)$ drift farther apart over time, meaning that the difference between the major radius M and equivalent radius R of the particles, and thus the aspect ratio A , increases.

To quantitatively grasp the changing ripening behavior, we give values for the apparent ripening exponent n as introduced in Eq. [6]. This quantity is determined by a least-square fit of Eq. [6] to the curves in Figure 4(a) with a fixed $\bar{S}(t_0)$ taken directly from the data and with $t_0 = 0$. The results of the fits are given in Table IV.

For the ripening of spherical precipitates, we find an apparent ripening exponent of $n = 2.8$. The expected value according to the LSW theory is 3. We conclude that the observed deviation of 0.2 is the precision with which the presented phase-field model allows to measure ripening exponents. This difference can be attributed to the fact that the original LSW theory does not account for finite volume contents and coalescence of precipitates. The phase-field model used in this work does not discriminate translational variants of the ordered phase. Coalescence of precipitates of different translational variants grow together under the formation of an anti-phase boundary. As this is not reflected in the used model, the rate of coalescence is overestimated. This higher rate of precipitate coalescence might cause the observed deviation from the exponent of 3. Further limitations of the methodology are the assumed isotropy of the interfacial energy and the single-variant microstructure of the simulation setup. Experimental observations indicate that ripening behavior is not influenced by the presence or dissolution of orientation variants of γ'' at constant volume fraction.^[59]

For ripening of plate-shaped precipitates, the apparent ripening exponents $n = 2.0$ and 1.7 are found. These are significantly lower compared to the ripening exponent of spherical precipitates considering the uncertainties discussed above. The difference between $n = 2.0$ and 1.7 is attributed to the increasing aspect ratio that leads to steadily increasing difference between the major radius of the plates and the equivalent radius. The temporal increase in the major radius thus exhibits less pronounced deceleration. The difference between

$n = 2.8$ and 2.0 is attributed to elastic effects from misfit strains.

Figure 5 shows the size dependence of the precipitate aspect ratios in the ripening simulations. The mean aspect ratio \bar{A} of the precipitates is plotted as function of their mean equivalent radius \bar{R} . The shape transition is illustrated by ellipses with aspect ratios and sizes to scale. For the spherical precipitates in the simulation without consideration of the misfit strains, the aspect ratio is always around unity. The mean aspect ratio of the plate-shaped precipitates increases with increasing precipitate size. The slope of the curve decreases with increasing precipitate size. This is in good accordance to observations of the shape of single precipitates^[2,8] and precipitates in regular arrangements.^[30] In the range from 10 to 30 nm equivalent radius, and 25 to 105 nm plate diameter, respectively, the mean aspect ratio can be approximated by least-square fitting a power law as

$$\bar{A} \approx 0.72\bar{Q}^{0.74}, \quad [18]$$

where $Q = R/L$ is the dimensionless precipitate size.

Figure 6 shows the diffusion potential of Nb at the phase boundary between matrix and γ'' precipitates. The diffusion potential is inhomogeneous due to the Gibbs–Thomson effect at curved interfaces (see Eq. [2]). High potentials are shown in red and lower

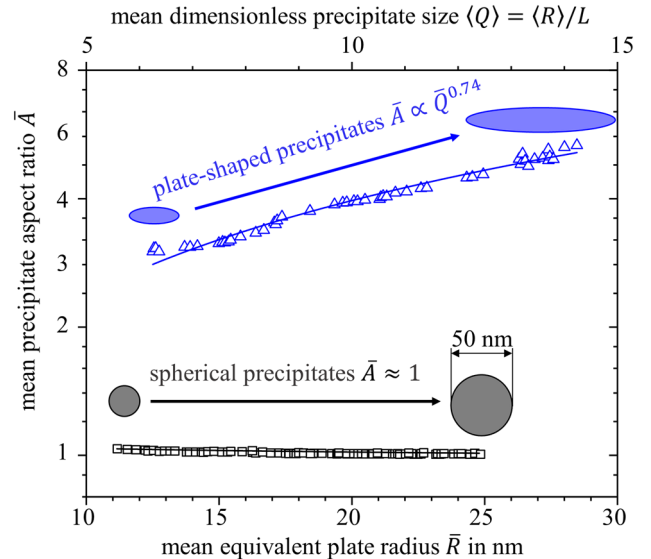


Fig. 5—Mean aspect ratio \bar{A} of the precipitates as a function of the mean precipitate equivalent radius \bar{R} for spherical and plate-shaped precipitates as measured from the 3D simulations with a power-law fit. The shape transition is depicted by ellipses.

Table IV. Results of fitting Eq. [6] to the simulated precipitate size over time from Fig. 4(a)

Lattice Misfit Strain	Definition of Precipitate Size S	Coefficient of Ripening K	$\bar{S}(t_0)$ in nm	Ripening Exponent n
$\varepsilon_c \gg \varepsilon_a, \varepsilon_b > 0$	major radius M	$2 \times 10^{-17} \text{ m}^{1.7} \text{ s}^{-1}$	12.4	1.7
	equiv. radius R	$7 \times 10^{-20} \text{ m}^{2.0} \text{ s}^{-1}$	10.5	2.0
$\varepsilon_a, \varepsilon_b, \varepsilon_c = 0$	sphere radius R	$3 \times 10^{-26} \text{ m}^{2.8} \text{ s}^{-1}$	10.5	2.8

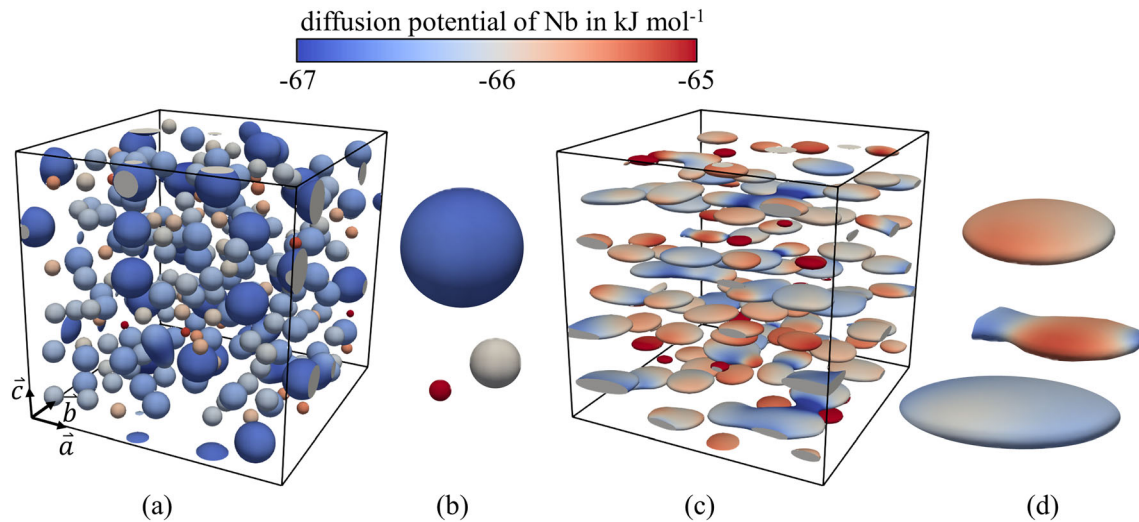


Fig. 6—Nb Diffusion potential at the interfaces of (a) and (b) spherical precipitates (c) and (d) Plate-shaped precipitates. (b) and (d) show representative distributions of the diffusion potential along precipitate interfaces.

potentials are blue. Ripening happens via diffusion from red interfaces towards blue interfaces. Figure 6(a) shows the distribution of the diffusion potential field at the interface of the spherical precipitates. The potential is significantly increased when precipitates are very small. This is due to the higher curvature κ of the interface of smaller precipitates as shown in Eq. [2]. Figure 6(b) shows three magnified precipitates with an even distribution of the interfacial potential. Figure 6(c) shows the interfacial diffusion potential in the case of plate-shaped precipitates. Smaller precipitates again show increased potential relative to larger ones so that a diffusional flow occurs that causes ripening. However, as emphasized in Figure 6(d), due to strongly inhomogeneous curvature of the interfaces, the diffusion potential is also distributed inhomogeneously along the interface. The lowest potentials are found on concave interfaces that form during the coalescence of precipitates. The ripening behavior in a system of strongly non-spherical precipitates is complex and the diffusion potential does not necessarily only coincide with the local curvature but depends also on the neighboring precipitates. This visualization illustrates the influence that the precipitate shape has on the ripening behavior.

B. Separation of the Elastic Effects that Influence the Precipitate Ripening Behavior

When the lattice misfit, and thus elastic stresses in precipitates and matrix, is considered in the phase-field model, the observed ripening exponent drops from 2.8 to 2.0. This elastic effect on the ripening behavior can be separated into one part that is independent of the precipitate shape and into a shape-dependent effect. The first part has been discussed in the previous contributions.^[52–54] The latter is due to the size dependence of the precipitate shape that is depicted in Figure 5. With increasing precipitate size, the aspect ratio of the precipitates increases which again leads to increased curvature of the interfaces and thus to accelerated

riping kinetics. It is not directly possible to separate the strength of both effects separately from phase-field simulations. In a spatially fully resolved model, both effects always occur together. For this reason, the argumentation on how the effect of size-dependent precipitate shapes influences the observed decrease of the apparent ripening exponent is based on the ripening law in Eq. [6]. The ripening law is extended to include size-dependent ripening kinetics. Equation [6] is formulated as a differential equation such that

$$\frac{\partial}{\partial t}(\bar{R}^k) = f_K(\bar{R}), \quad [19]$$

where the ripening coefficient is a function f_K of the mean precipitate size \bar{R} . The exponent k governs the ripening behavior at every time step independently of the effect of non-constant ripening kinetics. The exponent k thus includes the reduction of the ripening exponent due to misfit stresses but not due to the elastically induced size dependence of the precipitate shape. It is independent of the precipitate shape.

To include the non-constant ripening kinetics, we describe the ripening coefficient f_K as a power-law size dependence with an exponent m

$$f_K \propto \bar{R}^m. \quad [20]$$

This size dependence of the ripening kinetics is a direct consequence of the anisotropic lattice misfit of the precipitates. To elucidate this fact, we separate the relation in Eq. [20] into two separate dependencies. The first contribution is the size dependence of the precipitate shape that is caused by the interplay between interfacial and elastic contributions. This size dependence is observable in Figure 5 as the steady increase of the mean aspect ratio

$$\bar{A} \propto \bar{R}^z \quad [21]$$

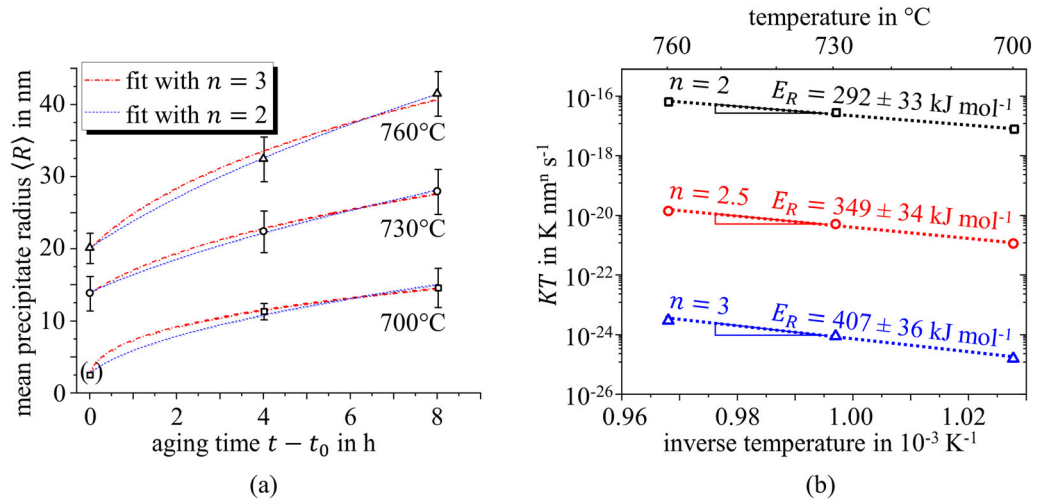


Fig. 7—(a) Experimental ripening data. Fits with $n = 2$ and 3 are given for each temperature. (b) Plot of $\ln(KT)$ over the inverse temperature for $n = 2, 2.5$ and 3 . The activation energies of ripening E_R are given for each assumed ripening exponent n .

with $\alpha \approx 0.74$ as given in Eq. [18].

The second contribution to the size dependence of the ripening kinetics is a shape dependence of the ripening kinetics. This effect is a consequence of the inhomogeneous curvature that all non-spherical precipitates exhibit. The Gibbs–Thomson effect is inhomogeneously strong at different points on a precipitates surface as it is demonstrated in Figure 6. The shape dependence of the ripening coefficient is also described by a power-law relation as a function of the mean aspect ratio

$$f_K \propto \bar{A}^\beta. \quad [22]$$

Kozeschnik *et al.* found $\beta = 2/3$ in the case of cylindrical precipitates with a constant aspect ratio.^[50] Boyd and Nicholson report a linear dependence on the aspect ratio for plate-shaped particles that have a plate radius equal to the radius of a sphere.^[8,49] Both findings are identical when the condition of equal precipitate volumes rather than equal radii is met.

The size dependence of the ripening kinetics is the nested relation of the size dependence of the precipitate shape in Eq. [21] and the shape dependence of the ripening kinetics in Eq. [22] such that we find

$$f_K \propto \bar{A}^\beta = (\bar{R}^\alpha)^\beta = \bar{R}^{\alpha\beta}. \quad [23]$$

The exponent m in Eq. [20] can then be defined as the product of α and β .

Under the assumption of a power-law size dependence of the ripening coefficient, we find the following solution to Eq. [19]:

$$\bar{R}(t)^{(k-m)} - \bar{R}(t_0)^{(k-m)} = \frac{k-m}{k} Ct = Kt. \quad [24]$$

Equation [24] is equivalent to the proposed heuristic approach in Eq. [6] with the apparent ripening exponent

being $n = k - m$ and $t_0 = 0$. This means that ripening with ever-increasing coefficient of ripening is equivalent to ripening with a decreased exponent of ripening. Note that in Eq. [24] mass is only conserved when R is the equivalent radius of spheres with the same volume as the precipitates.

The elastically induced size dependence of the ripening kinetics is expressed as two nested power-law relations with exponents α and β that together form the relation given in Eq. [20] with $m = \alpha\beta$. The power-law relation between f_K and \bar{R} fulfills the requirements that the ripening coefficient is steadily increasing with precipitate size. For the limit of spherical precipitates ($A \rightarrow 1$), a power-law yields unphysically inhibited ripening kinetics. This approach is therefore only valid for precipitates with a pronounced plate shape.

From Eq. [24] it becomes evident that a ripening coefficient that increases with the precipitate size ($m > 0$) lowers the apparent ripening exponent n . From Eq. [18] we already have a well-defined power-law approximation for the size dependence of the mean aspect ratio with $\alpha = 0.74$. To quantitatively grasp the decrease of the ripening exponent $n = k - m$ due to the size-dependent precipitate shape, we now investigate the exponent m . Due to the lack of a general description of the shape dependence of the ripening kinetics for shapes, we take $\beta = 2/3$ as the shape dependence of the ripening coefficient. We thus find an exponent of size dependence $m = \alpha\beta = 0.5$.

The difference between the ripening exponent of spherical precipitates without elastic misfit strains and the ripening exponent with consideration of these strains is around 0.8 (see Figure 4(a)). We explain more than 60 pct of the deviation of the ripening exponent by the elastically induced effect that the size-dependent precipitate shape has on the ripening kinetics. The remainder of the deviation from a ripening exponent of 3 is due to the effect of elastic misfit stresses that reduce the ripening exponent k independent of the precipitate shape.^[45,46,53] In accordance with the findings in

Figure 4(a), the exponent is $k = 2.5$. This is in good agreement with the reported value of 2.4 in a system with plate-shaped cubic precipitates with isotropic misfit.^[53] Considering the uncertainty of β , the exponent that governs the shape dependence of the ripening kinetics, we can state that the shape effect on the ripening behavior is of the same magnitude as the elastic effect that is shape-independent and is thus necessary to consider when modeling the Ostwald ripening behavior of plate-shaped tetragonal precipitates.

To assess the deviation between the ripening exponent of 1.7 that governs the temporal increase of the major radius M of the plates and the exponent of 2.0 that governs the evolution of the equivalent radius R of the precipitates, we assume an idealized precipitate shape of an oblate spheroid. In this case, the equivalent radius R and the major radius M are connected via $\bar{M}^3 = \bar{A} \cdot \bar{R}^3$.^[31] Given the relation between $\bar{A} \propto \bar{R}^{0.74}$ from Eq. [18] we find $\bar{M}^3 \propto \bar{R}^{3.74}$ which, solved for \bar{R} , yields a relation $\bar{R} \propto \bar{M}^{0.8}$. When \bar{R}^2 increases linearly with time, $\bar{M}^{1.6}$ will increase linearly with time as well. Within the accuracy of the measurement of the ripening exponents and considering the assumption of well-distributed perfect ellipses, this explains the lowered ripening exponent that was observed when the major radius M and not the equivalent radius R of the precipitates is evaluated. Accordingly, the exponent of ripening for the plate thickness M/A is 4, which is in very good agreement with the previous findings for plate-shaped misfitting precipitates.^[53]

C. Activation Energy of Ripening

Figure 7(a) shows experimentally observed mean precipitates sizes over a time of 8 hours at three temperatures $T = 700$ °C, 730 °C, and 760 °C. The time is chosen such that another 2 hours of initial aging have passed to only observe Ostwald ripening at equilibrium γ'' volume fraction and not the precipitation of γ'' from the supersaturated matrix (2 to 10 hours of aging in Figure 2). The data point with the smallest precipitate size at 700 °C is shown in brackets as the measured value is very close to the resolution of the SEM images. It is excluded from further analysis. To test the postulated square root time dependence of the precipitate ripening behavior, that was extracted from simulation data in Figure 4(a), we fit Eq. [6] to data from the aging experiments with fixed apparent ripening exponents n . For every temperature, two fits of Eq. [6] with $n = 2$ and $n = 3$ are shown. All fits have a coefficient of determination above 0.98.

The results of the ripening simulation shown in Figure 4(a) have a significantly stronger potential to reveal the ripening behavior of γ'' as they provide a continuous time series. A similarly dense set of ex-situ experimental data that allows conclusive determination of the ripening exponent requires immensely high reproducibility of the aging and subsequent quenching. Aging experiments over significantly longer times can help discriminate the ripening behavior but will be prone

to the formation of interfacial dislocations and transformation of γ'' to the stable δ phase. Both effects will significantly alter the ripening behavior beyond the effects discussed in this work. Similar uncertainty with direct comparison of experimental data under varying ripening exponents is reported for ripening of γ' precipitates.^[47] From the present experimental approach, it is therefore not directly possible to conclusively argue whether a ripening exponent of $n = 2$ or $n = 3$ is more justified.

The validity of the square root time dependence over the cube root can, however, be supported by the observed activation energy of ripening. The ripening coefficients K are obtained from least-square fits of Eq. [6] with different assumed ripening exponents n . Figure 7(b) shows plots of KT over the inverse temperature for assumed ripening exponents $n = 2, 2.5, \text{ and } 3$. The slopes in this plot correspond to the activation energy of ripening. Assuming a ripening behavior governed by an apparent ripening exponent of $n = 3$, the activation energy of ripening is 407 ± 36 kJ mol⁻¹. This value is of the same magnitude as the activation energies of diffusion in the alloy (see Table II), and we can thus conclude that the ripening is indeed diffusion controlled. The value is significantly larger than the activation energy of diffusion of Nb given in Table II that controls the ripening kinetics of γ'' . This leads to the conclusion that modeling the ripening behavior of γ'' precipitates with a ripening exponent of 3 is not physically conclusive.

When a smaller ripening exponent is assumed, we observe that the activation energy of ripening is decreasing. At $n = 2$ the activation energy drops to 292 ± 33 kJ mol⁻¹. This value is significantly closer to the activation energy that is reported for Nb in alloys 718 and 718 M. This observation indicates that an exponent smaller than 3 provides a more conclusive description of the ripening behavior.

V. SUMMARY AND CONCLUSION

We studied the ripening behavior of tetragonal phases that appear as coherent plate-shaped precipitates in a cubic matrix on the example of γ'' precipitates in alloy 718 M. 3D sharp phase-field simulations of Ostwald ripening were conducted with and without explicit consideration of elastic misfit strains in the material. The observed precipitate morphology is plate shaped or spherical, respectively. Plate-shaped particles exhibit a pronounced size dependence of their shape that causes the size-dependent ripening kinetics. By extending classical ripening laws to include a size-dependent ripening coefficient, we illustrated how the elastic misfit strains influence the ripening behavior of γ'' . The following conclusions are drawn:

1. The γ'' ripening behavior deviates significantly from the classical LSW theory. The apparent ripening exponent in 3D simulations is as low as 1.7 compared to the classically assumed value of 3. A

difference of 0.8 is entirely caused by elastic effects when a non-zero lattice misfit is considered.

- The simulation results are consistent to experimentally observed ripening behavior. Data from aging experiments are evaluated assuming different ripening exponents. It is revealed that exponents smaller than 3, as predicted by the simulations, yield significantly more conclusive activation energies of ripening.
- Between 700 °C and 760 °C, the Ostwald ripening of γ'' precipitates with plate diameters between 25 and 105 nm is best described by $\bar{R}(t)^2 - \bar{R}(t_0)^2 = K(t - t_0)$, where \bar{R} is the mean equivalent radius of the precipitates. The activation energy of ripening is 292 kJ mol⁻¹.
- The size dependence of the precipitate shapes causes a size dependence of the ripening kinetics. This elastically induced effect leads to the discussed reduction of the ripening exponent. 60 pct of the difference between the exponents is attributed to this shape effect. An additional difference of 0.3 is caused solely by the choice of measure of the precipitate size.

ACKNOWLEDGMENTS

This work is funded by the Deutsche Forschungsgemeinschaft (DFG) with grant numbers GL181/53-1, FL826/3-1, and FL826/5.

CONFLICT OF INTEREST

The authors declare that they have no conflict of interest.

FUNDING

Open Access funding enabled and organized by Projekt DEAL.

OPEN ACCESS

This article is licensed under a Creative Commons Attribution 4.0 International License, which permits use, sharing, adaptation, distribution and reproduction in any medium or format, as long as you give appropriate credit to the original author(s) and the source, provide a link to the Creative Commons licence, and indicate if changes were made. The images or other third party material in this article are included in the article's Creative Commons licence, unless indicated otherwise in a credit line to the material. If material is not included in the article's Creative Commons licence and your intended use is not permitted by statutory regulation or exceeds the permitted use, you will need

to obtain permission directly from the copyright holder. To view a copy of this licence, visit <http://creativecommons.org/licenses/by/4.0/>.

REFERENCES

- D.F. Paulonis, J.M. Oblak, and D.S. Duvall: *Am. Soc. Met. Trans. Quart.*, 1969, vol. 62, pp. 611–22.
- R. Cozar and A. Pineau: *Scr. Metall.*, 1973, vol. 7, pp. 851–54.
- A.J. Detor, R. DiDomizio, R. Sharghi-Moshtaghin, N. Zhou, R. Shi, Y. Wang, D.P. McAllister, and M.J. Mills: *Metall. Mater. Trans. A*, 2018, vol. 49A, pp. 708–17.
- R. Shi, D.P. McAllister, N. Zhou, A.J. Detor, R. DiDomizio, M.J. Mills, and Y. Wang: *Acta Mater.*, 2019, vol. 164, pp. 220–36.
- C.H. Zenk, L. Feng, D. McAllister, Y. Wang, and M.J. Mills: *Acta Mater.*, 2021, vol. 220, p. 117305.
- K. Kusabiraki, I. Hayakawa, S. Ikeuchi, and T. Ooka: *Iron and Steel*, 1994, pp. 348–52.
- Y.-Y. Lin, F. Schleifer, M. Fleck, and U. Glatzel: *Mater. Charact.*, 2020, vol. 165, p. 110389.
- A. Devaux, L. Nazé, R. Molins, A. Pineau, A. Organista, J.Y. Guédou, J.F. Uginet, and P. Héritier: *Mater. Sci. Eng. A*, 2008, vol. 486, pp. 117–22.
- X.S. Xie, J.X. Dong, and M.C. Zhang: *MSF*, 2007, vol. 539–543, pp. 262–69.
- J. He, S. Fukuyama, and K. Yokogawa: *J. Mater. Sci. Technol.*, 1994, vol. 17(3), pp. 302–08.
- C. Slama, C. Servant, and G. Cizeron: *J. Mater. Res.*, 1997, vol. 12, pp. 2298–316.
- M. Sundararaman, P. Mukhopadhyay, and S. Banerjee: *Metall. Trans.*, 1992, vol. 23A, pp. 2015–8.
- D. Jianxin, X. Xishan, and Z. Shouhua: *Scr. Metall. Mater.*, 1995, vol. 33, pp. 1933–40.
- Y.-F. Han, P. Deb, and M.C. Chaturvedi: *Met. Sci.*, 1982, vol. 16, pp. 555–62.
- I.J. Moore, M.G. Burke, and E.J. Palmiere: *Acta Mater.*, 2016, vol. 119, pp. 157–66.
- N. Zhou, D.C. Lv, H.L. Zhang, D. McAllister, F. Zhang, M.J. Mills, and Y. Wang: *Acta Mater.*, 2014, vol. 65, p. 270.
- M.R. Tonks and L.K. Aagesen: *Annu. Rev. Mater. Res.*, 2019, vol. 49, pp. 79–102.
- D. Tourret, H. Liu, and J. LLorca: *Prog. Mater. Sci.*, 2022, p. 100810.
- Z. Yu, X. Wang, F. Yang, Z. Yue, and J.C.M. Li: *Crystals*, 2020, vol. 10, p. 1095.
- M. Holzinger, F. Schleifer, U. Glatzel, and M. Fleck: *Euro. Phys. J. B*, 2019, vol. 92, p. 208.
- B. Bhadak, R. Sankarasubramanian, and A. Choudhury: *Metall. Mater. Trans. A*, 2018, vol. 49A, pp. 5705–26.
- B. Bhadak, R.K. Singh, and A. Choudhury: *Metall. Mater. Trans. A*, 2020, vol. 51A, pp. 5414–31.
- V. Vaithyanathan, C. Wolverton, and L.Q. Chen: *Phys. Rev. Lett.*, 2002, vol. 88, p. 125503.
- N. Ta, M. U. Bilal, I. Häusler, A. Saxena, Y.-Y. Lin, F. Schleifer, M. Fleck, U. Glatzel, B. Skrotzki, and R. Darvishi Kamachali: *Materials*, 2021, vol. 14.
- Y.-Y. Lin, F. Schleifer, M. Holzinger, N. Ta, B. Skrotzki, R. Darvishi Kamachali, U. Glatzel, and M. Fleck: *Materials*, 2021, vol. 14.
- F. Schleifer, M. Fleck, M. Holzinger, Y.-Y. Lin, and U. Glatzel: *Superalloys 2020*, Ed. by S. Tin, M. Hardy, J. Clews, J. Cormier, Q. Feng, J. Marcin, C. O'Brien, and A. Suzuki, Springer, Cham, 2020, pp. 500–08.
- R. Lawitzki, S. Hassan, L. Karge, J. Wagner, D. Wang, J. von Kobylinski, C. Krempaszky, M. Hofmann, R. Gilles, and G. Schmitz: *Acta Mater.*, 2019, vol. 163, pp. 28–39.
- R.Y. Zhang, H.L. Qin, Z.N. Bi, J. Li, S. Paul, T.L. Lee, S.Y. Zhang, J. Zhang, and H.B. Dong: *Metall. Mater. Trans. A*, 2020, vol. 51A, pp. 1860–73.
- P.W. Voorhees, G.B. McFadden, and W.C. Johnson: *Acta Metall. Mater.*, 1992, vol. 40, pp. 2979–92.

30. F. Schleifer, M. Holzinger, Y.-Y. Lin, U. Glatzel, and M. Fleck: *Intermetallics*, 2020, vol. 120, p. 106745.
31. F. Schleifer, M. Müller, Y.-Y. Lin, M. Holzinger, U. Glatzel, and M. Fleck: *Integr. Mater. Manuf. Innov.*, 2022, vol. 11, pp. 159–71.
32. Peter Fratzl, Oliver Penrose, and Joel L. Lebowitz: *Journal of Statistical Physics*, 1999, vol. 95.
33. Y.C. Lin, X.-Y. Jiang, S.-C. Luo, and D.-G. He: *Mater. Des.*, 2018, vol. 139, pp. 16–24.
34. P.W. Voorhees: *J. Stat. Phys.*, 1985, vol. 38, p. 231.
35. I.M. Lifshitz and V.V. Slyosov: *J. Phys. Chem. Sol.*, 1961, vol. 19, p. 35.
36. C. Wagner: *Z. Elektrochem.*, 1961, vol. 65, p. 581.
37. M.R. Ahmadi, M. Rath, E. Povoden-Karadeniz, S. Primig, T. Wojcik, A. Danninger, M. Stockinger, and E. Kozeschnik: *Model. Simul. Mater. Sci. Eng.*, 2017, vol. 25, p. 55005.
38. K. Kim and P.W. Voorhees: *Acta Mater.*, 2018, vol. 152, pp. 327–7.
39. J.O. Andersson, T. Helander, L. Höglund, P. Shi, and B. Sundman: *Calphad*, 2002, vol. 26, pp. 273–312.
40. M.J. Sohrabi and H. Mirzadeh: *Met. Mater. Int.*, 2020, vol. 26, pp. 326–32.
41. M. Karunaratne and R.C. Reed: *DDF*, 2005, vol. 237–240, pp. 420–25.
42. A.J. Ardell: *Acta Metall.*, 1972, vol. 20, pp. 61–71.
43. I.J. Moore, M.G. Burke, N.T. Nuhfer, and E.J. Palmiere: *J. Mater. Sci.*, 2017, vol. 52, pp. 8665–0.
44. D. Bardel, M. Perez, D. Nelias, A. Deschamps, C.R. Hutchinson, D. Maisonnette, T. Chaise, J. Garnier, and F. Bourlier: *Acta Mater.*, 2014, vol. 62, pp. 129–40.
45. L.T. Mushongera, M. Fleck, J. Kundin, F. Querfurth, and H. Emmerich: *Adv. Eng. Mater.*, 2015, vol. 17, p. 1149.
46. W.C. Johnson, T.A. Abinandanan, and P.W. Voorhees: *Acta Metall. Mater.*, 1990, vol. 38, pp. 1349–67.
47. A.J. Ardell and V. Ozolins: *Nat. Mater.*, 2005, vol. 4, pp. 309–16.
48. X. Li, K. Thornton, Q. Nie, P.W. Voorhees, and J.S. Lowengrub: *Acta Mater.*, 2004, vol. 52, pp. 5829–43.
49. J.D. Boyd and R.B. Nicholson: *Acta Metall.*, 1971, vol. 19, p. 1379.
50. E. Kozeschnik, J. Svoboda, and F.D. Fischer: *Mater. Sci. Eng. A*, 2006, vol. 441, pp. 68–72.
51. M.E. Thompson and P.W. Voorhees: *Acta Mater.*, 1999, vol. 47, pp. 983–6.
52. V. Vaithyanathan and L.Q. Chen: *Acta Mater.*, 2002, vol. 50, pp. 4061–73.
53. Alphonse Finel: *Phase Transformations and Evolution in Materials*, Ed. by P. E. A. Turchi and A. Gonis, 2000, pp. 371–85.
54. Brener, Marchenko, Muller-Krumbhaar, and Spatschek: *Physical Review Letters*, 2000, vol. 84, pp. 4914–17.
55. M. Fleck and F. Schleifer: *Engineering with Computers*, 2022.
56. A. Finel, Y. Le Bouar, B. Dabas, B. Appolaire, Y. Yamada, and T. Mohri: *Phys. Rev. Lett.*, 2018, vol. 121, p. 25501.
57. M. Fleck, F. Schleifer, M. Holzinger, and U. Glatzel: *Metall. Mater. Trans. A*, 2018, vol. 49A, pp. 4146–57.
58. F. Theska, A. Stanojevic, B. Oberwinkler, S.P. Ringer, and S. Primig: *Acta Mater.*, 2018, vol. 156, pp. 116–24.
59. H. Qin, Z. Bi, R. Zhang, T. L. Lee, H. Yu, H. Chi, D. Li, H. Dong, J. Du, and J. Zhang: *Superalloys 2020*, Ed. by S. Tin, M. Hardy, J. Clews, J. Cormier, Q. Feng, J. Marcin, C. O'Brien, and A. Suzuki, Springer International Publishing, Cham, 2020, pp. 713–25.

Publisher's Note Springer Nature remains neutral with regard to jurisdictional claims in published maps and institutional affiliations.